

REST-FRAME OPTICAL PROPERTIES OF LUMINOUS $1.5 < z < 3.5$ QUASARS: THE $H\beta$ -[O III] REGION

YUE SHEN¹

Draft version June 25, 2021

ABSTRACT

We study the rest-frame optical properties of 74 luminous ($L_{\text{bol}} = 10^{46.2-48.2} \text{ erg s}^{-1}$), $1.5 < z < 3.5$ broad-line quasars with near-IR (*JHK*) slit spectroscopy. Systemic redshifts based on the peak of the [O III] $\lambda 5007$ line reveal that redshift estimates from the rest-frame UV broad emission lines (mostly Mg II) are intrinsically uncertain by $\sim 200 \text{ km s}^{-1}$ (measurement errors accounted for). The overall full-width-at-half-maximum of the narrow [O III] line is $\sim 1000 \text{ km s}^{-1}$ on average. A significant fraction of the total [O III] flux ($\sim 40\%$) is in a blueshifted wing component with a median velocity offset of $\sim 700 \text{ km s}^{-1}$, indicative of ionized outflows within a few kpc from the nucleus; we do not find evidence of significant [O III] flux beyond $\sim 10 \text{ kpc}$ in our slit spectroscopy. The [O III] line is noticeably more asymmetric and weaker than that in typical less luminous low- z quasars. However, when matched in quasar continuum luminosity, low- z quasars have similar [O III] profiles and strengths as these high- z systems. Therefore the exceptionally large width and blueshifted wing, and the relatively weak strength of [O III] in high- z luminous quasars are mostly a luminosity effect rather than redshift evolution. The $H\beta$ -[O III] region of these high- z quasars displays a similar spectral diversity and Eigenvector 1 correlations with anti-correlated [O III] and optical Fe II strengths, as seen in low- z quasars; but the average broad $H\beta$ width is larger by 25% than typical low- z quasars, indicating more massive black holes in these high- z systems. These results highlight the importance of understanding [O III] in the general context of quasar parameter space in order to understand quasar feedback in the form of [O III] outflows. The calibrated one-dimensional near-IR spectra are made publicly available, along with a composite spectrum.

Keywords: black hole physics – galaxies: active – line: profiles – quasars: general

1. INTRODUCTION

Recent development of high-throughput near-IR spectrographs on moderate- to large-aperture telescopes has enabled the study of the rest-frame optical properties of high-redshift ($z > 1.5$) quasars (e.g., McIntosh et al. 1999; Yuan & Wills 2003; Shemmer et al. 2004; Netzer et al. 2004; Sulentic et al. 2004, 2006). Over the past decade or so, the sample of high-redshift quasars with near-IR spectroscopy has grown considerably in size, and started to explore the statistical properties of the narrow-line regions (NLRs) and rest-frame optical broad-line regions (BLRs) of high-redshift quasars and their possible evolution from their low-redshift counterparts.

Near-IR spectroscopy of high- z quasars provides a broad range of important applications, from estimating their black hole (BH) masses using the single-epoch virial BH mass estimators (for a recent review, see Shen 2013) based on the most reliable Balmer lines (e.g., Dietrich et al. 2002; Dietrich & Hamann 2004; Netzer et al. 2004; Sulentic et al. 2004, 2006; Dietrich et al. 2009; Greene et al. 2010; Assef et al. 2011; Ho et al. 2012; Shen & Liu 2012; Runnoe et al. 2013b; Zuo et al. 2015; Brotherton et al. 2015a; Plotkin et al. 2015; Shemmer & Lieber 2015; Saito et al. 2015), to studying the sizes and kinematics of the NLR (usually utilizing the strong [O III] $\lambda\lambda 4959, 5007$ line) at $z > 1.5$ (e.g., Netzer et al. 2004; Nesvadba et al. 2008; Kim et al. 2013; Brusa et al. 2015; Perna et al. 2015; Carniani et al. 2015). A wide wavelength coverage combining optical and near-IR spectroscopy of quasars is also valuable for constraining the spectral energy distribution (SED) of quasars and for testing accretion disk models (e.g., Capellupo et al.

2015).

The sizes and kinematics of the NLR of low- z Seyfert galaxies and quasars have been studied extensively in the past (e.g., Mulchaey et al. 1996; Bennert et al. 2002; Schmitt et al. 2003; Bennert et al. 2006a,b). These studies suggest that the NLR size increases with quasar luminosity, although there is evidence for an upper limit of $\sim 10 \text{ kpc}$ on the NLR size for the most luminous quasars (e.g., Netzer et al. 2004; Hainline et al. 2014). In recent years, interests on NLR gas distributions and kinematics have been revived in the context of quasar-driven outflows and feedback from BH accretion. The [O III] emission in low- z Seyferts and quasars often shows significant blueshifted velocity components indicative of outflows (e.g., Heckman et al. 1981; Whittle 1985; Antonucci 2002), and spatial extensions beyond $\sim \text{kpc}$ scales, as inferred from spatially resolved slit or integral-field-unit (IFU) spectroscopy (e.g., Stockton & MacKenty 1987; Crenshaw & Kraemer 2000; Nelson et al. 2000; Fu & Stockton 2009; Fischer et al. 2010; Villar-Martín et al. 2011; Greene et al. 2011; Shen et al. 2011b; Liu et al. 2013a,b; Husemann et al. 2013). Such kinematic studies of the NLR have been recently extended to $z > 1.5$ for small samples with spatially-resolved near-IR spectroscopy (e.g., Nesvadba et al. 2008; Harrison et al. 2012; Brusa et al. 2015; Perna et al. 2015; Carniani et al. 2015), which suggest that quasar-driven outflows in ionized [O III] gas are common in luminous high- z quasars.

On the other hand, the rest-frame UV-to-optical regime of quasars displays a well-organized spectral diversity, which is ultimately connected to the fundamental properties of BH accretion. The most prominent feature of the quasar spectral diversity is a collection of quantities that all correlate with the strength of the optical Fe II emission known as Eigenvector 1 (EV1), discovered by Boroson & Green (1992). In

¹ Department of Astronomy and National Center for Supercomputing Applications, University of Illinois at Urbana-Champaign, Urbana, IL 61801, USA; shenyue@illinois.edu

the optical, one of the most important EV1 correlations is the anti-correlation between the strengths of [O III] and Fe II, even when quasar luminosity is fixed. EV1 has been the focus of quasar phenomenology for the past two decades (e.g., Boroson & Green 1992; Wang et al. 1996; Boller et al. 1996; Brotherton 1996; Laor 1997, 2000; Wills et al. 1999; Sulentic et al. 2000; Marziani et al. 2001; Boroson 2002; Shang et al. 2003; Netzer et al. 2007; Sulentic et al. 2007; Dong et al. 2011; Shen & Ho 2014; Sun & Shen 2015), as it provides important clues to understanding quasar accretion and feedback processes. It has been suggested that the main physical driver of EV1 is the Eddington ratio of the BH accretion (e.g., Boroson & Green 1992; Sulentic et al. 2000; Boroson 2002; Dong et al. 2011; Shen & Ho 2014; Sun & Shen 2015), although other effects (such as orientation) may still play a minor role in affecting the observed strength of the [O III] lines (e.g., Risaliti et al. 2011). In addition to the EV1 correlation, the [O III] line also shows a Baldwin effect (Baldwin 1977), i.e., the restframe equivalent width (REW) of [O III] decreases as continuum luminosity increases (e.g., Brotherton 1996; Zhang et al. 2011; Stern & Laor 2012a,b), often accompanied by increasing flux in the blueshifted [O III] wing (e.g., Zhang et al. 2013). Shen & Ho (2014) presented a comprehensive analysis of the [O III] properties in low- z quasars, and showed that the strength of the core [O III] component decreases with quasar luminosity and optical Fe II strength faster than the wing [O III] component, leading to overall broader and more blueshifted [O III] profiles as luminosity and Fe II strength increases. However, the blueshifted [O III] component appears to be a ubiquitous feature among quasars at different luminosities (see figs. 2, E1 and E2 in Shen & Ho 2014).

Building on these results on low- z quasars, a natural step forward is to extend such studies to $z > 1.5$ with near-IR spectroscopy to cover the rest-frame optical regime, and to investigate if these correlations involving [O III] and other optical lines exist at earlier times. However, compared with optical spectroscopy, near-IR spectroscopy of faint high- z targets is much more expensive, and hence most of the earlier near-IR spectroscopic studies of high- z quasars are still limited either by small sample statistics (of order ten objects or less) or by low spectral quality (i.e., low S/N, low spectral resolution, and/or limited spectral coverage). To enable a robust statistical study, high-quality near-IR spectroscopy for a large sample of high- z quasars is therefore desirable.

We have been conducting a near-IR spectroscopic survey of $1.5 < z < 3.5$ quasars to study their rest-frame optical properties. Shen & Liu (2012) presented a study on the correlations among virial mass estimators based on the UV broad lines and optical broad Balmer lines using 60 quasars at $z \sim 1.5 - 2.2$ from this survey. Here we present 14 additional quasars at $z \sim 3.5$ with new near-IR spectroscopy, and use a total of 74 quasars to study the rest-frame optical properties of these high- z quasars, focusing on [O III] properties and EV1 correlations that involve the $H\beta$ -[O III] region. In §2 we describe the sample and spectral measurements, with a discussion on the systemic redshift estimation. We present our results in §3 and discussions in §4, and conclude in §5. Throughout the paper we adopt a flat Λ CDM cosmology with $\Omega_0 = 0.3$ and $H_0 = 70 \text{ km s}^{-1} \text{ Mpc}^{-1}$. We use the REW to refer to the strength of a particular emission line.

2. DATA AND SPECTRAL MEASUREMENTS

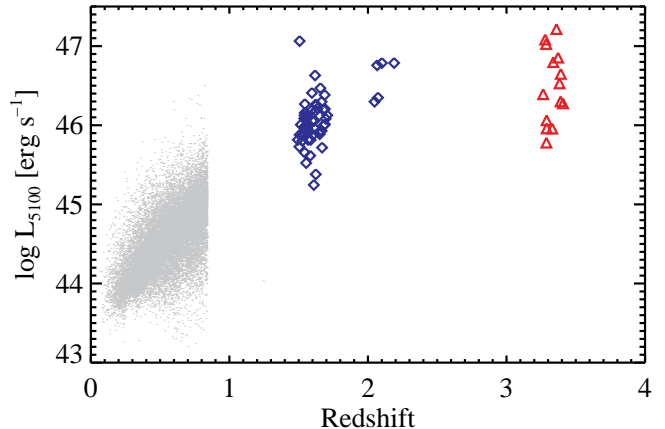


Figure 1. Distribution of our near-IR quasar sample (open symbols) in the redshift-luminosity plane. For comparison, we show the distribution of the low- z SDSS sample from Shen et al. (2011a) with $H\beta$ -[O III] coverage.

2.1. Sample

Our sample of quasars with near-IR spectroscopy consists of the 60 quasars at $z \sim 1.5 - 2.2$ from Shen & Liu (2012), and 14 additional quasars at $z \sim 3.3$ for which we have obtained near-IR spectroscopy with the Folded-port InfraRed Echellett (FIRE; Simcoe et al. 2010) on the 6.5 m Magellan-Baade telescope during two runs in May and Dec, 2013. Table 1 summarizes the basic information of the 14 new $z \sim 3.3$ quasars. The data reduction and flux calibration of the new FIRE spectroscopy followed the same procedure as described in Shen & Liu (2012). All 74 quasars have simultaneous JHK coverage in the near-IR. These quasars were selected from the SDSS DR7 quasar catalog (Shen et al. 2011a) with good optical spectra covering the CIV line and in redshift windows of $z \sim 1.5, 2.1, 3.3$ such that the $H\beta$ -[O III] region can be covered in the JHK bands in the near-IR. Requiring them to have good quality (S/N per pixel $\gtrsim 10$) SDSS spectra preferentially selects high-luminosity quasars at these redshifts, but the resulting sample still covers a range of spectral diversities in the emission line properties. Most of these quasars are radio-quiet (Shen et al. 2011a).

Fig. 1 shows the distribution of our sample in the redshift-luminosity plane, compared to the low- z quasar sample drawn from SDSS DR7 (Shen et al. 2011a) with optical spectroscopy covering the $H\beta$ -[O III] region. We have applied an average correction for host contamination in the rest-frame 5100 Å luminosities for the low- z comparison sample, using the empirical formula in Shen et al. (2011a, eqn. 1). There is no need to apply this correction for the luminous quasars in our near-IR sample.

The reduced and calibrated 1d near-IR spectra for all 74 quasars used in this study are available in ASCII format in the online version of the paper.

2.2. Spectral Measurements

We use functional fits to measure the continuum and emission line properties of our near-IR quasar sample following earlier work (e.g., Shen et al. 2008, 2011a) in the $H\beta$ -[O III] region covered by near-IR spectroscopy. In short, we fit a local power-law continuum plus an empirical optical Fe II template (Boroson & Green 1992) to the wavelength regions just outside the $H\beta$ -[O III] complex to form a pseudo-continuum. We then subtract this pseudo-continuum model from the original spectrum, and fit a number of Gaussian func-

Table 1
New near-IR spectroscopic data

Object Name (1)	RA (J2000) (2)	DEC (J2000) (3)	Plate (4)	Fiber (5)	MJD (6)	z_{sys} (7)	i_{PSF} (8)	$J_{2\text{MASS}}$ (9)	$H_{2\text{MASS}}$ (10)	$K_{s,2\text{MASS}}$ (11)	NIR Obs. (12)	Obs. UT (13)
J0250-0757	02 50 21.77	-07 57 50.0	0457	261	51901	3.3376	17.99	16.7	16.1	15.9	FIRE	131228
J0259+0011	02 59 05.64	+00 11 21.9	0411	398	51817	3.3724	17.75	16.2 (16.43)	15.5 (15.83)	15.2 (15.18)	FIRE	131230
J0304-0008	03 04 49.86	-00 08 13.5	0411	153	51817	3.2859	17.47	16.3 (16.22)	15.7 (15.86)	15.3 (15.21)	FIRE	131229
J0352-0517	03 52 20.70	-05 17 02.7	2071	353	53741	3.2892	18.73	17.6	0.0	0.0	FIRE	131230
J0810+0936	08 10 11.97	+09 36 48.3	2421	214	54153	3.3906	18.35	17.4	0.0	16.2	FIRE	131229
J0843+0750	08 43 12.64	+07 50 29.3	1298	376	52964	3.2648	19.22	16.9 (17.82)	0.0 (17.24)	0.0 (16.50)	FIRE	131229
J0844+0503	08 44 01.96	+05 03 57.9	1188	464	52650	3.3603	17.09	15.4 (15.46)	14.9 (15.00)	14.2 (14.24)	FIRE	131228
J0910+0237	09 10 54.79	+02 37 04.6	0566	014	52238	3.2902	18.56	17.3 (17.57)	16.1 (17.13)	0.0 (16.57)	FIRE	131230
J0942+0422	09 42 02.05	+04 22 44.5	0570	427	52266	3.2790	17.18	15.9 (15.75)	15.3 (15.23)	14.6 (14.58)	FIRE	131228
J0953+0336	09 53 33.71	+03 36 23.7	0571	114	52286	3.2881	19.85	17.4 (18.27)	0.0 (17.74)	0.0 (17.23)	FIRE	131230
J0954+0915	09 54 34.94	+09 15 19.6	1306	052	52996	3.4076	18.67	17.4 (17.44)	16.5 (17.11)	0.0 (16.61)	FIRE	131230
J1019+0254	10 19 08.27	+02 54 31.9	0503	456	51999	3.3829	18.03	16.7 (16.72)	16.2 (16.38)	15.5 (15.76)	FIRE	131229
J1034+0358	10 34 56.31	+03 58 59.4	0576	026	52325	3.3918	17.69	16.4 (16.43)	15.8 (15.95)	15.4 (15.36)	FIRE	131229
J2238-0921	22 38 19.77	-09 21 06.0	0722	190	52224	3.3300	17.81	16.7	16.2	15.5	FIRE	130529

NOTE. — Summary of the 14 new SDSS quasars at $z \sim 3.3$ for which we have obtained near-infrared spectroscopy. Columns (4)-(6): plate, fiber and MJD of the optical SDSS spectrum for each object; (7): systemic redshift determined from the near-IR spectrum (see §2.2); (8): SDSS i -band PSF magnitudes; (9)-(11): 2MASS magnitudes (Vega) and UKIDSS (Lawrence et al. 2007) magnitudes (Vega) in the parentheses when available; (12): instrument for the near-IR spectroscopy; (13): UT dates of the near-IR observations. Note that here the 2MASS magnitudes were taken from Schneider et al. (2010), where aperture photometry was performed upon 2MASS images to detect faint objects, hence these near infrared data go beyond the 2MASS All-Sky and “6×” point source catalogs (see Schneider et al. 2010, for details); zero values indicate non-detections.

tions (in logarithmic wavelength space) to model the broad and narrow emission lines. We used 3 Gaussians to describe the broad $H\beta$ and 1 Gaussian to describe the narrow $H\beta$. The $[O\text{III}]\lambda\lambda 4959, 5007$ doublet was each modeled by two Gaussians, one for the “core” component and one for the blueshifted “wing” component. During the fit, the velocity shift and dispersion of the narrow $H\beta$ component are tied to those of the “core” component of $[O\text{III}]$.

We determine the systemic redshift z_{sys} using the model peak of the full $[O\text{III}]\lambda 5007$ profile; in cases where $[O\text{III}]$ is not covered or if its S/N is poor, we use the model peak from the $H\beta$ line. Fig. 2 compares these systemic redshifts with those reported by Hewett & Wild (2010) (z_{HW}), which were based on cross-correlations of rest-frame UV lines (mostly Mg II for most of our objects) with quasar templates and empirical corrections for the velocity offsets between UV lines and the systemic redshifts. There is a small mean offset of $\sim 100\text{ km s}^{-1}$ between z_{HW} and z_{sys} and a dispersion of $\sim 280\text{ km s}^{-1}$ between the two redshifts. The reported measurement uncertainties in the Hewett & Wild redshifts are typically $\sim 180\text{ km s}^{-1}$, while the typical measurement uncertainty in our systemic redshift estimates is $\sim 60\text{ km s}^{-1}$. Subtracting the typical measurement uncertainties, there is a residual difference of $\sim 200\text{ km s}^{-1}$ in the two sets of redshifts, which reflects the systematic uncertainty in estimating the systemic redshifts based on rest-frame UV lines (mostly Mg II for the bulk of our near-IR sample). This systematic uncertainty in Mg II-based redshifts is consistent with that inferred from comparing Mg II and $[O\text{III}]$ -based redshifts in low- z SDSS quasars using the spectral measurements in Shen et al. (2011a). The refined systemic redshifts for the near-IR sample are important for deriving the composite spectrum and studying the average line profile of these objects.

We note that for the bulk of the population the peak of the full $[O\text{III}]$ is consistent to within $\sim 50\text{ km s}^{-1}$ with the systemic redshifts based on stellar absorption lines (e.g., Hewett & Wild 2010; Bae & Woo 2014) or low-ionization

lines such as $[S\text{II}]$ (e.g., Zhang et al. 2011) or $[O\text{II}]$ (e.g., Shen & Ho 2014), although rare individual objects could have a large blueshifted velocity offset in the $[O\text{III}]$ peak (e.g., Zamanov et al. 2002; Boroson 2005; Komossa et al. 2008). However, if a single Gaussian were fit to the overall $[O\text{III}]$ profile, the potential blueshifted “wing” component could bias the redshift estimation based on the Gaussian peak.

On the other hand, Hewett & Wild (2010) suggested that, based on the analysis of low- z quasar spectra, the $[O\text{III}]$ centroid measured above the 50 per cent peak-height level², is on average blueshifted from systemic (defined by Ca II K line at 3934.8 \AA) by $\sim 45\text{ km s}^{-1}$. Taken this mean offset of $[O\text{III}]$ into account, the comparison shown in Fig. 2 suggests that the Mg II-based redshifts in Hewett & Wild (2010) only mildly overestimate the systemic redshifts by $\sim 50\text{ km s}^{-1}$ on average for our quasars.

We measure the continuum luminosity at rest-frame 5100 \AA and the emission line properties (such as the rest-frame equivalent width REW and FWHM) using the model fits. To estimate measurement errors, we use a Monte Carlo approach (e.g., Shen et al. 2008, 2011a): for each object we perturb the original spectrum by adding artificial noise using the reported spectral error array to generate a mock spectrum and perform the same fit on it; we repeat the process for 50 realizations of mock spectra and record the measurements for each realization; the nominal 1σ measurement errors are then estimated as the semi-amplitude of the range enclosing the 16th and 84th percentiles of the distribution from the mock spectra. We provide a fits catalog of the spectral measurements in the $H\beta$ - $[O\text{III}]$ region for our near-IR sample and documented the catalog in Table 3. Additional properties of these quasars can be found in the Shen et al. (2011a) catalog.

3. RESULTS

² This is slightly different from our approach of measuring the $[O\text{III}]$ peak velocity from model fits.

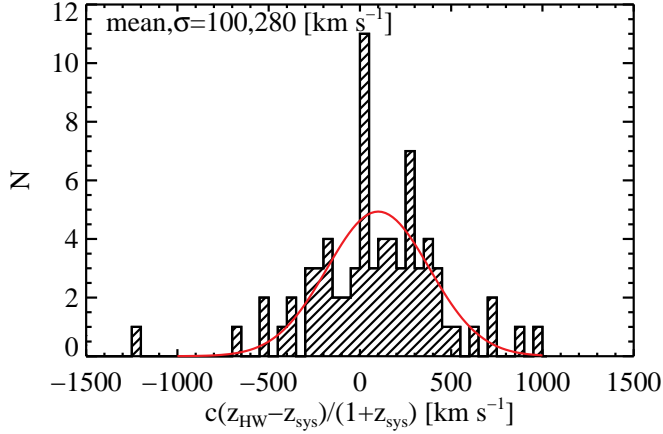


Figure 2. Histogram of the differences (with measurement errors) between the HW redshifts based on rest-frame UV lines (mostly Mg II) and the systemic redshifts based on [O III] (or H β) for our near-IR sample. The red line is a best-fit Gaussian to the distribution, with the mean and dispersion shown. The HW redshifts are on average larger than the [O III] (H β)-based systemic redshifts by $\sim 100 \text{ km s}^{-1}$.

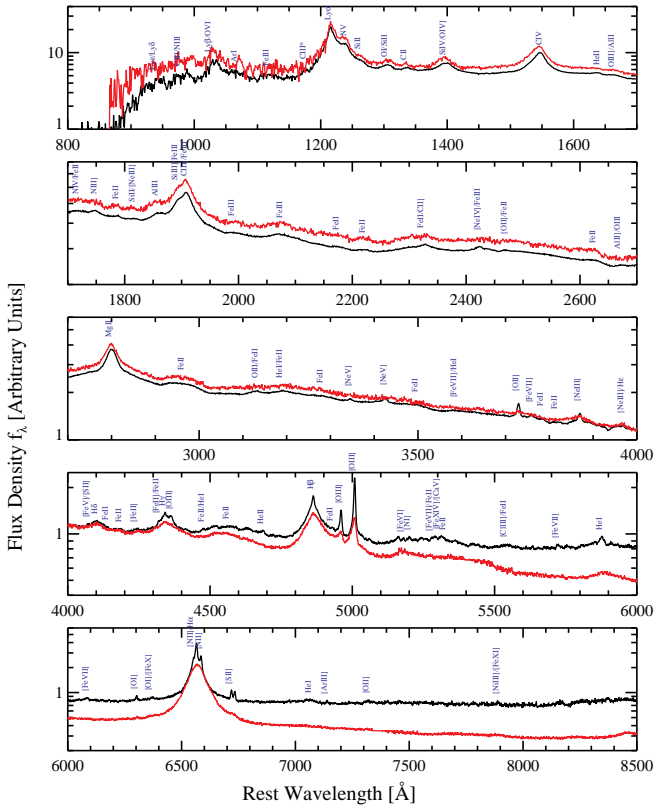


Figure 3. Median composite spectra for our near-IR sample (red) and for SDSS quasars from Vanden Berk et al. (2001, black). Other than the apparently broader emission line profiles and the bluer continuum (see text), the composite spectrum for the high- z quasars is similar to that of general SDSS quasars. The full composite spectrum for the near-IR sample is tabulated in Table 2.

3.1. Composite Spectrum of the Near-IR Sample

We create a composite spectrum of our near-IR sample combining optical SDSS and near-IR spectroscopy. We follow Vanden Berk et al. (2001) to create a median composite spectrum, which better preserves the relative strengths of emission lines. The full composite spectrum is shown

Table 2
Composite Spectrum

Rest Wavelength	Flux	Flux Error	N_{obj}
(1)	(2)	(3)	(4)
800.5	0.000	0.000	0
801.5	0.000	0.000	0

NOTE. — Median composite spectrum for our near-IR quasar sample. Wavelengths are in units of \AA . Flux and flux error units are arbitrary. The last column indicates how many objects contributed to the median composite at each wavelength pixel.

in Fig. 3 and compared to the SDSS quasar composite in Vanden Berk et al. (2001). Our composite is slightly bluer than the Vanden Berk et al. (2001) composite, which may be caused by our selection of objects with relatively blue continua typical of classical quasars, but a more likely explanation is that our luminous quasars are much less affected by host contamination than the low- z and low-luminosity quasars used in the Vanden Berk et al. composite at rest-frame optical wavelengths (see discussions in Shen et al. 2011a). One advantage of our composite is that all objects contributed to the wavelength coverage, whereas the Vanden Berk et al. composite used high- z /high-luminosity quasars to cover the rest-frame UV and low- z /low-luminosity quasars to cover the rest-frame optical. This explains why the two composite spectra have similar UV broad-line properties but different optical line properties. The use of the Vanden Berk et al. composite for high- z quasars should caution on the potential impact of host contamination in the composite.

Although we only have a small number of objects contributing to the rest-frame optical regime, we clearly detect several weak narrow lines such as [O I] and [S II], which will be used to probe the physical properties of the NLRs of these high- z quasars in future work. These detected weak narrow lines appear to be substantially broader than those in the composite spectrum generated for low- z quasars. In addition, the broad H β and H α lines also appear broader than the low- z composite. These results are consistent with the fact that our near-IR sample represents the most luminous quasars and thus likely more massive hosts than low- z quasars, hence both the broad lines and the narrow lines have larger widths than their low- z counterparts with less massive BHs and hosts.

The full composite spectrum for our near-IR sample is tabulated in Table 2.

3.2. Strength and Kinematics of [O III]

We were able to measure [O III] $\lambda 5007$ for all but one of our objects, although for $\sim 35\%$ of them [O III] $\lambda 5007$ is not detected at $> 3\sigma$ significance. Only for one object (J0412–0612) [O III] $\lambda 5007$ is not covered in our near-IR spectroscopy. Fig. 4 (left) shows the [O III] $\lambda 5007$ REW as a function of continuum luminosity, where we also plot the low- z SDSS quasars for comparison. The scatter in the [O III] $\lambda 5007$ REW is large for our high- z quasar sample, but there is no obvious indication that the distribution is bimodal. The average [O III] $\lambda 5007$ strength is consistent with earlier near-IR spectroscopic studies on smaller samples of quasars with similar luminosities and redshifts as studied here (e.g., Sulentic et al. 2004; Netzer et al. 2004).

The average trend of decreasing [O III] $\lambda 5007$ REW with luminosity as shown in Fig. 4 (left) is known as the [O III] Baldwin effect (e.g., Baldwin 1977; Brotherton 1996; Zhang et al.

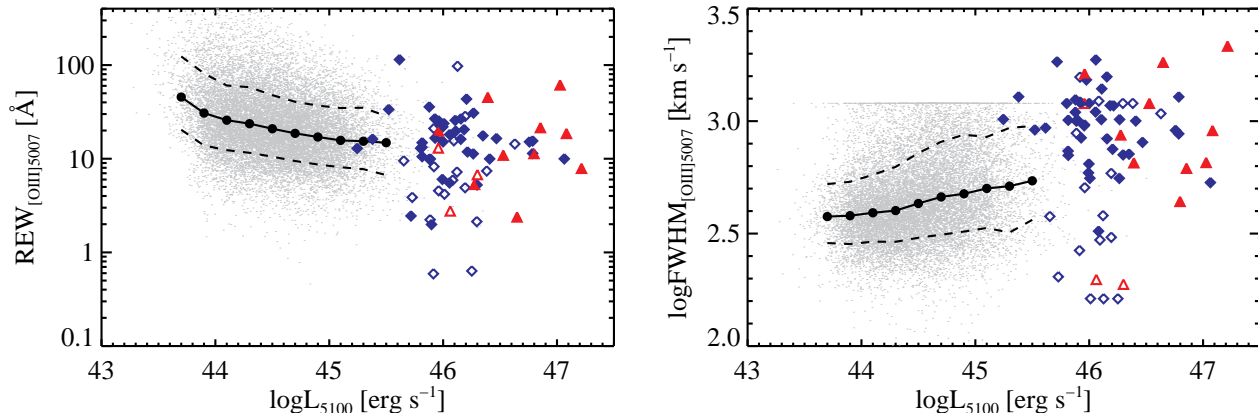


Figure 4. Comparisons between our high- z quasars (diamonds and triangles) and the $z < 1$ SDSS quasars (gray dots), where the latter measurements are from Shen et al. (2011a). *Left:* the total [O III] equivalent width as a function of the rest-frame 5100 Å continuum luminosity. *Right:* the FWHM of the entire [O III] profile as a function of L_{5100} . Symbol notations are the same as in Fig. 1. The lines are the 16th, 50th and 84th percentiles of the distribution of low- z SDSS quasars. The open symbols are those with low-quality [O III] detections ($S/N < 3$). We caution that individual measurements for the near-IR sample can be quite noisy (see Table 3). The pileup of gray points at the top in the right panel is due to the upper limit of 1200 km s^{-1} imposed in the [O III] fits in Shen et al. (2011a).

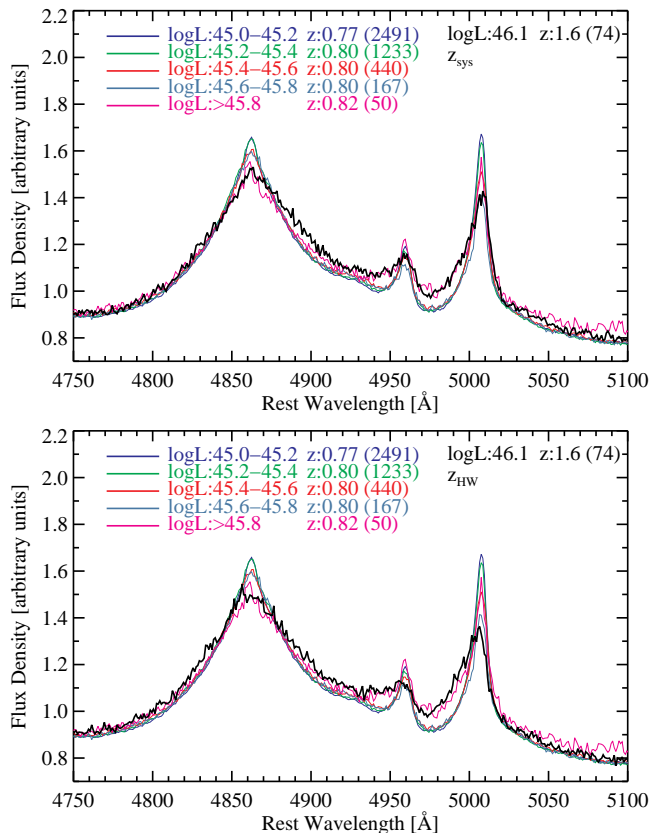


Figure 5. Median composite spectra of the $z > 1.5$ near-IR quasar sample (black lines) and comparison with the composite spectra of the most luminous low- z SDSS quasars in different luminosity bins. *Top:* Using the estimated systemic redshifts z_{sys} for the near-IR sample. *Bottom:* Using the redshifts reported by Hewett & Wild (2010) for the near-IR sample. The Hewett & Wild redshifts appear to be overestimated on average for the near-IR sample, and have an additional scatter relative to the systemic redshifts from [O III] (and H β).

2013; Stern & Laor 2012a,b). Shen & Ho (2014) showed that the [O III] $\lambda 5007$ Baldwin effect is primarily driven by the flux reduction in the “core” component of [O III] $\lambda 5007$ when quasar luminosity increases. A byproduct of this effect is the increase in the overall [O III] $\lambda 5007$ width, as the broad “wing” component becomes more prominent at higher lumi-

nosities (e.g., Shen & Ho 2014).

Recent near-IR spectroscopy of $z > 1.5$ luminous quasars (unobscured or obscured) often report exceptionally large [O III] widths, with $\text{FWHM} \gtrsim 1000 \text{ km s}^{-1}$ (e.g., Netzer et al. 2004; Kim et al. 2013; Brusa et al. 2015). Fig. 4 (right) shows the FWHM of the full [O III] $\lambda 5007$ profile and compares with the low- z SDSS quasar sample. The median [O III] $\lambda 5007$ FWHM is $\sim 1000 \text{ km s}^{-1}$ for our near-IR sample, confirming the large FWHM values found in earlier work (e.g., Netzer et al. 2004; Kim et al. 2013; Brusa et al. 2015). However, despite the large scatter in our sample, they tend to follow the luminosity trend extrapolated from less luminous objects at lower redshifts. This suggests that the NLR kinematics of $z > 1.5$ quasars is not significantly different from those at lower redshifts with similar quasar luminosities.

To strengthen the above point, we use the median composite spectrum generated for our near-IR sample (§3.1), and compare it to the median composite spectra of low- z SDSS quasars in different luminosity bins in Fig. 5. When luminosity is matched, our high- z sample shows a similar average [O III] profile as the most luminous low- z quasars, suggesting there is limited redshift evolution in terms of [O III] properties when luminosity is matched. For comparison, in the bottom panel of Fig. 5, we show the resulting median composite spectrum using the Hewett & Wild redshifts for our high- z quasars. The composite shows an additional broadening due to the systematic uncertainty in the Hewett & Wild redshifts based on broad UV lines. In addition, the peak of [O III] in the Hewett & Wild composite is blueshifted from that in the composite based on systemic redshifts by $\sim 2 \text{ \AA}$ (rest-frame), consistent with the result in §2.2 and Fig. 2 that the Hewett & Wild redshifts (mostly Mg II-based) on average overestimate the [O III]-based systemic redshifts by $\sim 100 \text{ km s}^{-1}$ for our near-IR sample.

High-luminosity quasars display a strong blueshifted component in their [O III] emission (e.g., Shen & Ho 2014). We have used a simple decomposition method to decompose the [O III] emission into a core component and a blueshifted wing component. The median fraction of the blueshifted wing component to the total [O III] flux is $\sim 40\%$. The wing component for our near-IR sample shows a broad range of blueshift velocities of up to $\sim 1200 \text{ km s}^{-1}$, and has a median blueshift

Table 3
Spectral Measurements

Column	Format	Units	Description
OBJNAME	A10	–	Object Name
PLATE	LONG	–	Plate number of the SDSS spectrum
FIBER	LONG	–	Fiber ID of the SDSS spectrum
MJD	LONG	–	Modified Julian Date of the SDSS spectrum
RA	DOUBLE	degree	J2000 Right ascension
DEC	DOUBLE	degree	J2000 Declination
ZHW	FLOAT	–	Redshift from Hewett & Wild (2010)
ZHW_ERR	FLOAT	–	Measurement error in ZHW
ZSYS	FLOAT	–	Systemic redshift
ZSYS_ERR	FLOAT	–	Measurement error in ZSYS
LOGL5100	DOUBLE	[erg s ⁻¹]	Continuum luminosity at rest-frame 5100 Å
LOGL5100_ERR	DOUBLE	[erg s ⁻¹]	Measurement error in LOGL5100
FWHM_BROAD_HB	DOUBLE	km s ⁻¹	FWHM of the broad Hβ component
FWHM_BROAD_HB_ERR	DOUBLE	km s ⁻¹	Measurement error in FWHM_BROAD_HB
EW_BROAD_HB	DOUBLE	Å	Rest-frame equivalent width of the broad Hβ component
EW_BROAD_HB_ERR	DOUBLE	Å	Measurement error in EW_BROAD_HB
LOGL_BROAD_HB	DOUBLE	[erg s ⁻¹]	Luminosity of the broad Hβ component
LOGL_BROAD_HB_ERR	DOUBLE	[erg s ⁻¹]	Measurement error in LOGL_BROAD_HB
LOGL_NARROW_HB	DOUBLE	[erg s ⁻¹]	Luminosity of the narrow Hβ component
LOGL_NARROW_HB_ERR	DOUBLE	[erg s ⁻¹]	Measurement error in LOGL_NARROW_HB
EW_OIII_5007	DOUBLE	Å	Rest-frame equivalent width of the entire [O III] λ5007 line
EW_OIII_5007_ERR	DOUBLE	Å	Measurement error in EW_OIII_5007_ERR
LOGL_OIII_5007	DOUBLE	[erg s ⁻¹]	Luminosity of the entire [O III] λ5007 line
LOGL_OIII_5007_ERR	DOUBLE	[erg s ⁻¹]	Measurement error in LOGL_OIII_5007
LOGL_OIII_5007C	DOUBLE	[erg s ⁻¹]	Luminosity of the core component of [O III] λ5007
LOGL_OIII_5007C_ERR	DOUBLE	[erg s ⁻¹]	Measurement error in LOGL_OIII_5007C
LOGL_OIII_5007W	DOUBLE	[erg s ⁻¹]	Luminosity of the wing component of [O III] λ5007
LOGL_OIII_5007W_ERR	DOUBLE	[erg s ⁻¹]	Measurement error in LOGL_OIII_5007W
FWHM_OIII_5007	DOUBLE	km s ⁻¹	FWHM of the entire [O III] λ5007 line
FWHM_OIII_5007_ERR	DOUBLE	km s ⁻¹	Measurement error in FWHM_OIII_5007
FWHM_OIII_5007C	DOUBLE	km s ⁻¹	FWHM of the core component of [O III] λ5007
FWHM_OIII_5007C_ERR	DOUBLE	km s ⁻¹	Measurement error in FWHM_OIII_5007C
FWHM_OIII_5007W	DOUBLE	km s ⁻¹	FWHM of the wing component of [O III] λ5007
FWHM_OIII_5007W_ERR	DOUBLE	km s ⁻¹	Measurement error in FWHM_OIII_5007W
VOFF_OIII_5007W	DOUBLE	km s ⁻¹	Velocity offset of the wing component of [O III] λ5007 from systemic (negative means blueshift)
VOFF_OIII_5007W_ERR	DOUBLE	km s ⁻¹	Measurement error in VOFF_OIII_5007W
EW_FE_4434_4684	DOUBLE	Å	Rest-frame equivalent width of the optical Fe II complex within 4434-4684 Å
EW_FE_4434_4684_ERR	DOUBLE	Å	Measurement error in EW_FE_4434_4684
LOGBH_HB_VP06	FLOAT	[M _⊙]	Single-epoch BH mass estimate based on broad Hβ (Vestergaard & Peterson 2006)
LOGBH_HB_VP06_ERR	FLOAT	[M _⊙]	Measurement error in LOGBH_HB_VP06 (systematic error not included)

NOTE. — Format of the fits table containing the Hβ-[O III] region spectral measurements of our sample. The full table is available in FITS format in the online version of the paper.

of $\sim 700 \text{ km s}^{-1}$, much larger than the $\sim 200 \text{ km s}^{-1}$ average blueshift of the wing component in much less luminous low- z quasars ($L_{5100} \sim 10^{44} \text{ erg s}^{-1}$) (e.g., Zhang et al. 2011; Shen & Ho 2014). However, Shen & Ho (2014) showed that the blueshift velocity of the wing component increases with quasar luminosity, and the observed $\sim 700 \text{ km s}^{-1}$ velocity at the high luminosity regime sampled by our quasars ($L_{5100} \sim 10^{46} \text{ erg s}^{-1}$) is consistent with simple extrapolation from the luminosity trend found by Shen & Ho (2014, their Fig. E2).

3.3. Aperture Effects and NLR Sizes

Our near-IR spectra were obtained using two different instruments: TripleSpec (Wilson et al. 2004) on the ARC 3.5 m telescope (38 quasars), and FIRE on the 6.5 m Magellan-Baade telescope (36 quasars including the 14 quasars at $z \sim 3.3$). The TripleSpec observations used a slit width of either $1.1''$ or $1.5''$, and the FIRE observations used a slit width of $0.6''$. In both cases the slit was positioned at the parallac-

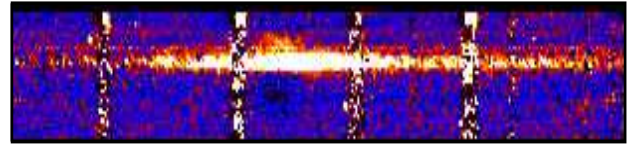


Figure 6. The rectified 2D spectrum in the [O III] λ5007 region for J1220+0004 from FIRE. Vertical is the slit direction, which covers $\sim 6''$ along the slit. Horizontal is the wavelength direction, covering rest-frame 4970–5050 Å. The local continuum has been subtracted using a crude polynomial fit to pixels outside the [O III] λ5007 region. Most of the [O III] flux is concentrated within the central $\sim 1''$. For this particular object there is evidence (the fluffy feature above the central emission) that some extended [O III] flux exists beyond the central $\sim 1''$, which, however, does not contribute to the total [O III] flux significantly.

tic angle in the middle of the observation. Since the major axis of the NLR is at random with respect to the slit position, our near-IR spectra on average enclose a physical region with comparable sizes to the slit width. Given the angular scale of $\sim 8.5 \text{ kpc}''$ (at $z \sim 1.6$) and $\sim 7.5 \text{ kpc}''$ (at $z \sim 3.3$), our

near-IR spectra enclose all [O III] flux within $\sim 5 - 10$ kpc. Therefore the blueshifted wing [O III] component revealed in our spectra, if originated from quasar-driven outflows, is constrained to be within a few kpc from the nucleus. Future adaptive optics (AO) assisted near-IR IFU observations will improve the constraints on the spatial extent of this blueshifted [O III] component in luminous $z > 1.5$ quasars.

We also expect that aperture losses due to the finite slit widths used are not important for our near-IR quasars. Netzer et al. (2004) showed that there is little [O III] flux beyond $\sim 1''$ radius (~ 7 kpc) in their slit near-IR spectra of high- z quasars, which have similar luminosities and redshifts as our objects. With their careful analysis on the long-slit optical spectroscopy of $0.4 < z < 0.7$ type 2 quasars, Hainline et al. (2014) showed that there is an upper limit of ~ 7 kpc on the size of the NLR in luminous quasars. Since the surface brightness of [O III] emission typically decreases with distance (e.g., Liu et al. 2013a), it is reasonable to expect that our aperture already encloses most of the [O III] flux, and the observed Baldwin effect is intrinsic and not subject to increasing aperture losses as quasar luminosity increases.

To further ensure that we are not missing significant [O III] flux beyond our slit aperture, we visually inspected all 2D spectra for our objects. We found that in essentially all but 2–3 cases the [O III] flux is concentrated within the central $\sim 1''$ in the slit direction, and is consistent with being unresolved under the seeing conditions (e.g., similar spatial profiles for [O III] and continuum emission). In these 2–3 exceptions we see evidence that some extended [O III] emission exist beyond the central $\sim 1''$, but even in such cases the contribution of these extended emission to the total [O III] flux is negligible. An example of extended [O III] emission in our high- z quasars is shown in Fig. 6. We therefore confirm the earlier result in Netzer et al. (2004) that most of the [O III] flux in luminous $z > 1.5$ quasars is within ~ 10 kpc from the nucleus. However, to perform a detailed analysis on the spatial extent of the [O III] emission using our slit spectroscopy requires more careful spectral reductions/calibrations and a proper treatment of seeing effects, and is beyond the scope of the current work.

3.4. Eigenvector 1 Relations

As mentioned in §1, another important spectral quantity that regulates the strength and width of [O III] $\lambda 5007$ is the optical Fe II strength (e.g., the EV1 correlations). These spectral correlations are governed by simple underlying physical processes of the BH accretion. Early near-IR spectroscopic studies on small samples already hinted that similar EV1 correlations may exist in high-redshift quasars (e.g., Sulentic et al. 2004, 2006; Runnoe et al. 2013b).

Fig. 7 shows the anti-correlation between [O III] strength and optical Fe II strength, defined as $R_{\text{FeII}} \equiv \text{REW}_{\text{[OIII]}\lambda 5007} / \text{REW}_{\text{H}\beta, \text{broad}}$. Our near-IR quasars, although focused on the most luminous quasars, still shows a broad range of Fe II strength, and they fall consistently on the relation defined by the low- z quasars (black lines), albeit with slightly lower [O III] REW given the Baldwin effect discussed earlier. Therefore we confirm earlier results (e.g., Sulentic et al. 2004, 2006) that similar EV1 correlations already exist at $z > 1.5$ with our much larger sample.

Fig. 8 shows the locations of our near-IR quasars in the 2D EV1 plane defined by the Fe II strength R_{FeII} and the broad H β FWHM (e.g., Boroson & Green 1992; Sulentic et al. 2000; Shen & Ho 2014). Notably our high-luminosity near-IR quasars show a systematic offset in the broad H β FWHM,

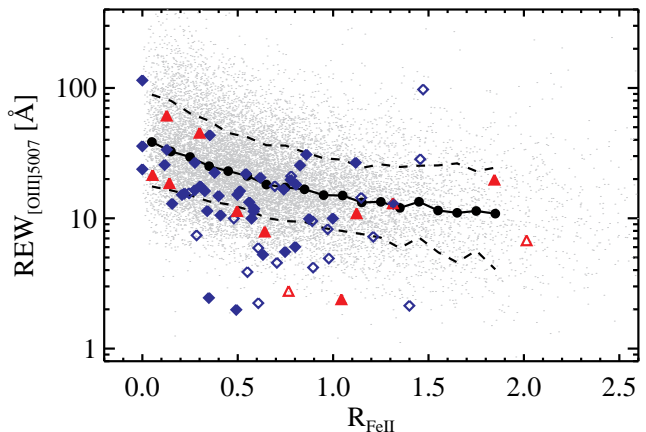


Figure 7. The anti-correlation between the [O III] EW and the optical Fe II strength (the EV1 relation). Symbol notations are the same as in Fig. 4. The gray points are for the low- z SDSS quasars in the Shen et al. (2011a) catalog, and the black lines indicate the median, 16th and 84th percentiles of the distribution. Our $z > 1.5$ quasars spread a similar range in optical Fe II strength, and follow the same EV1 trend defined by low- z quasars.

compared to the low- z SDSS quasars (contours). The median broad H β FWHM is ~ 5000 km s $^{-1}$ for our high- z sample and ~ 4000 km s $^{-1}$ for low- z SDSS quasars. This is consistent with our findings with the composite spectrum, and again indicates that these most luminosity quasars have larger BH masses than their low- z and low-luminosity counterparts. We note that the vertical dispersion of objects in Fig. 8 is primarily an orientation effect, based on the results of low- z quasars (e.g., Shen & Ho 2014; Sun & Shen 2015, also see Marziani et al. 2001). Such an orientation bias in the broad H β FWHM is also argued based on radio-loud quasars, where the orientation of the radio jet (hence the accretion disk and BLR orientation) can be inferred from the radio core dominance (e.g., Wills & Browne 1986; Runnoe et al. 2013a; Brotherton et al. 2015b).

4. DISCUSSION

The strong blueshifted [O III] components and the exceptionally broad [O III] FWHMs observed in our broad-line quasars are consistent with recent studies of different types of AGN (e.g., ultraluminous infrared galaxies ULIRGs/AGN and obscured quasars, radio-loud and radio-quiet quasars) at similar redshifts and luminosities (e.g., Harrison et al. 2012; Kim et al. 2013; Brusa et al. 2015). In particular, Harrison et al. (2012) observed eight $z = 1.4 - 3.4$ ULIRGs hosting AGN activity with near-IR integral field spectroscopy, and found evidence of broad [O III] emission on several kpc scales with velocity offsets of up to ~ 850 km s $^{-1}$. The FWHM, velocity offset and spatial extent of the [O III] emitting gas in their ULIRG/AGN sample are consistent with those inferred from our slit spectroscopy for luminous broad-line quasars (see §3). Our results, along with these recent studies, suggest that kpc-scale outflows in ionized gas are common among the most luminous high-redshift actively accreting SMBHs.

Brusa et al. (2015) presented near-IR spectroscopy for 8 obscured quasars at $z \sim 1.5$ and measured [O III] properties for 6 of them. Their obscured quasars have bolometric luminosities $\sim 10^{45-46.5}$ erg s $^{-1}$, about a factor of ~ 10 lower than those for our quasars, but are still among the luminous quasar population. Consistent with our results here, they reported large [O III] widths and velocity offsets for their small

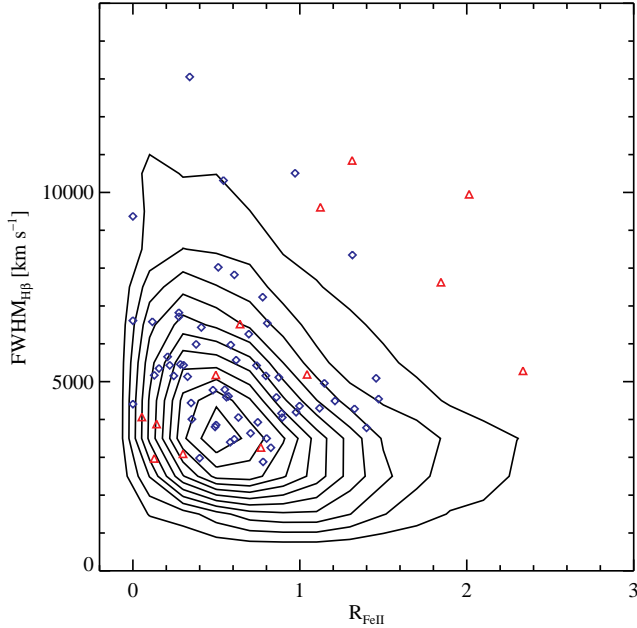


Figure 8. Distribution of our near-IR sample in the EV1 plane defined by R_{FeII} and the broad $\text{H}\beta$ FWHM. The contours are for the low- z and low-luminosity SDSS quasars based on the measurements in Shen et al. (2011a). The high- z near-IR sample shows a similar wedged distribution, but the broad $\text{H}\beta$ FWHMs are offset to systematically larger values, which is consistent with the scenario that these most luminous quasars also have more massive BHs than their low-luminosity counterparts. Symbol notations are the same as in Fig. 1.

sample. They also performed a comprehensive comparison of the $[\text{O III}]$ FWHM among different populations of active SMBHs, and found that their $z \sim 1.5$ obscured quasars have substantially larger $[\text{O III}]$ FWHMs than those in $z < 0.6$ type 2 quasars with similar $[\text{O III}]$ luminosities. However, one potential caveat is that the $[\text{O III}]$ properties in quasars (strength and profile) are also strong functions of continuum luminosity and EV1 (e.g., Shen & Ho 2014), so systems with matched $[\text{O III}]$ luminosities may still have different physical properties such as quasar continuum luminosity or Eddington ratio.³ When matching the quasar continuum luminosity for our high- z quasars and for low- z SDSS quasars, we do not observe difference in their $[\text{O III}]$ properties, suggesting negligible redshift evolution in the $[\text{O III}]$ properties, at least in the most luminous unobscured broad-line quasars.

We note that while significant $[\text{O III}]$ flux beyond ~ 10 kpc is rare for our objects, there are exceptions at low redshift, such as extended $[\text{O III}]$ emission at tens of kpc in both radio-loud and radio-quiet quasars (obscured and unobscured) (e.g., Fu & Stockton 2009; Greene et al. 2011; Shen et al. 2011b; Fu et al. 2012; Husemann et al. 2013), some of which may be due to mergers. Since our slit spectroscopy may miss such extended $[\text{O III}]$ emission along other directions, a systematic search for extended $[\text{O III}]$ emission in the general population of $z > 1.5$ quasars with near-IR IFU observations is highly desirable.

It is interesting to note that a recent study of cool gas in quasar hosts at $z \sim 1$ traced by Mg II absorption imprinted on background quasar spectra (Johnson et al. 2015) also revealed

³ Different selections, e.g., $[\text{O III}]$ -based low- z type 2 quasar selection versus X-ray selected high- z obscured quasars, may also introduce additional complications in the comparison of their sample $[\text{O III}]$ properties.

a luminosity dependence of the Mg II-absorption gas covering fraction and velocity offset. Although the spatial extent of the Mg II-absorption gas in these low- z quasars is much larger than that of the $[\text{O III}]$ emission probed by our near-IR spectroscopy, and the luminosities of these $z \sim 1$ quasars are much lower than those of our high- z quasars, it is possible that there is a connection between gas outflows on \sim kpc scales and on larger scales, as suggested by the similar luminosity trends seen in the two studies with different gas tracers.

5. CONCLUSIONS

We have performed a detailed study on the rest-frame optical properties (focusing on the $\text{H}\beta$ - $[\text{O III}]$ region) of $1.5 < z < 3.5$ luminous ($L_{\text{bol}} = 10^{46.2-48.2} \text{ erg s}^{-1}$) broad-line quasars, using a large sample of 74 objects with our own near-IR spectroscopy. The findings from this study are the following:

- The redshifts of these high- z quasars based on the UV broad lines (mostly Mg II) are uncertain by $\sim 200 \text{ km s}^{-1}$ compared to the more reliable systemic redshifts from the peak of the narrow $[\text{O III}]$ lines. In addition, the improved redshifts for SDSS-DR7 quasars by Hewett & Wild (2010) using broad UV lines are systematically biased high by $\sim 100 \text{ km s}^{-1}$ from the $[\text{O III}]$ -based redshifts for our quasars.
- The $[\text{O III}]$ strength is lower than that for typical SDSS quasars at $z < 1$, with a median REW of $\sim 13 \text{ \AA}$. Our high- z objects tend to follow the same Baldwin effect of decreasing $[\text{O III}]$ REW with quasar continuum luminosity as defined by low- z quasars.
- The $[\text{O III}]$ profile of these luminous quasars is highly asymmetric, with $\sim 40\%$ of the total flux in a blueshifted wing component on average. The wing component is on average blueshifted by $\sim 700 \text{ km s}^{-1}$ from the systemic velocity. The overall $[\text{O III}]$ width is exceptionally large, with a median FWHM $\sim 1000 \text{ km s}^{-1}$. These results confirm earlier observations with smaller near-IR spectroscopic samples at these redshifts (e.g., Netzer et al. 2004).
- However, we found that the strength and profile of $[\text{O III}]$ of these high- z luminous quasars are similar to those of their low- z counterparts with comparable quasar continuum luminosity, and they follow the extrapolated trends with luminosity defined by the less luminous low- z quasars. Therefore we conclude that the extreme properties of $[\text{O III}]$ in these high- z quasars are mainly driven by quasar luminosity rather than redshift evolution.
- Even within the limited dynamic range in quasar luminosity of our high- z sample, we observe a similar spectral diversity in terms of the optical Fe II strength and the well known EV1 correlations for low- z quasars. This suggests that the same physical processes that drive the diversity of quasars are already in place in these earlier active SMBHs. On the other hand, the average broad $\text{H}\beta$ FWHM is larger than that of the low- z and lower-luminosity quasars, reflecting the larger BH masses in these high- z quasars.
- Our slit spectroscopy suggests that most of the $[\text{O III}]$ flux in our objects is within the central ~ 10 kpc, and

the blueshifted [O III] wing component must also originate from below such spatial scales. We only found a handful of objects showing evidence of extended (but insignificant) [O III] emission beyond the central ~ 10 kpc covered in our slit spectra, which will be good targets for spatially-resolved follow-up observations (such as adaptive optics assisted near-IR IFU observations).

The average values and spread in the [O III] REW and FWHM in luminous high- z quasars presented here serve as a useful reference for planning near-IR spectroscopy to cover the [O III] region in high- z quasars (e.g., to obtain a reliable redshift estimate based on [O III]). The relatively weaker (due to the Baldwin effect) and broader width of [O III] of these high-luminosity quasars compared to typical low- z and low-luminosity quasars means that it is more difficult to detect and measure [O III] accurately for these luminous objects.

We have concluded that these luminous $1.5 < z < 3.5$ quasars are not different from their low- z counterparts at similar quasar continuum luminosities, in terms of the [O III] properties. The diversities in [O III] strength and kinematics are already clearly seen in recent studies using $z < 1$ SDSS quasars (e.g., Stern & Laor 2012a,b; Zhang et al. 2011, 2013; Shen & Ho 2014). In particular, we point out that blueshifted [O III] components are not unique to the most luminous quasars – they are ubiquitous among quasars, with their properties (e.g., the fraction to total [O III] flux, velocity offset and width) correlated with quasar parameters (luminosity and Eddington ratio, e.g., Shen & Ho 2014, figs. E1 and E2). Many recent studies use the kinematics of [O III] in different types of active galaxies to argue for AGN-driven outflows and feedback. Therefore it is important to understand the properties of [O III] emission in the general context of quasar parameter space, in order to understand the physical mechanisms driving these outflows. For example, the correlations of [O III] profile with both quasar continuum luminosity and optical Fe II strength (see fig. 2 and fig. E2 in Shen & Ho 2014) suggest that simple accretion parameters (luminosity and Eddington ratio) may play the primary role in regulating the behaviors of [O III] outflows.

I thank the referee for comments that led to improvement of the manuscript, and Xin Liu and Luis Ho for useful discussions. Funding for the SDSS and SDSS-II has been provided by the Alfred P. Sloan Foundation, the Participating Institutions, the National Science Foundation, the U.S. Department of Energy, the National Aeronautics and Space Administration, the Japanese Monbukagakusho, the Max Planck Society, and the Higher Education Funding Council for England. The SDSS Web Site is <http://www.sdss.org/>.

Facilities: Sloan, Magellan:Baade (FIRE), ARC (Triple-Spec)

REFERENCES

- Abazajian, K. N., et al. 2009, *ApJS*, 182, 543
 Antonucci, R. 2002, *Astrophysical Spectropolarimetry* (Cambridge Univ. Press), 151
 Assef, R. J., et al. 2011, *ApJ*, 742, 93
 Bae, H.-J., & Woo, J.-H. 2014, *ApJ*, 795, 30
 Baldwin, J. A. 1977, *ApJ*, 214, 679
 Bennert, N., Falcke, H., Schulz, H., Wilson, A. S., & Wills, B. J. 2002, *ApJ*, 574, L105
 Bennert, N., Jungwiert, B., Komossa, S., Haas, M., & Chini, R. 2006a, *A&A*, 456, 953
 Bennert, N., Jungwiert, B., Komossa, S., Haas, M., & Chini, R. 2006b, *A&A*, 459, 55
 Boller, T., Brandt, W. N., & Fink, H. 1996, *A&A*, 305, 53
 Boroson, T. A. & Green, R. F. 1992, *ApJS*, 80, 109
 Boroson, T. A. 2002, *ApJ*, 565, 78
 Boroson, T. 2005, *AJ*, 130, 381
 Brotherton, M. S. 1996, *ApJS*, 102, 1
 Brotherton, M. S., Runnoe, J. C., Shang, Z., & DiPompeo, M. A. 2015a, *MNRAS*, 451, 1290
 Brotherton, M. S., Singh, V., & Runnoe, J. 2015b, *MNRAS*, arXiv:1509.06468
 Brusa, M., Bongiorno, A., Cresci, G., Perna, M., Marconi, A., et al. 2015, *MNRAS*, 446, 2394
 Capellupo, D. M., et al. 2015, *MNRAS*, 446, 3427
 Carniani, S., Marconi, A., Maiolino, R., et al. 2015, *A&A*, 580, A102
 Crenshaw, D. M., & Kraemer, S. B. 2000, *ApJ*, 532, L101
 Dietrich, M., Appenzeller, I., Vestergaard, M., & Wagner, S. J. 2002, *ApJ*, 564, 581
 Dietrich, M., & Hamann, F. 2004, *ApJ*, 611, 761
 Dietrich, M., Mathur, S., Grupe, D., & Komossa, S. 2009, *ApJ*, 696, 1998
 Dong, X., et al. 2011, *ApJ*, 736, 86
 Fischer, T. C., Crenshaw, D. M., Kraemer, S. B., Schmitt, H. R., & Trippe, M. L. 2010, *AJ*, 140, 577
 Fu, H., Yan, L., Myers, A. D., et al. 2012, *ApJ*, 745, 67
 Fu, H., & Stockton, A. 2009, *ApJ*, 690, 953
 Greene, J. E., Peng, C. Y., & Ludwig, R. R. 2010, *ApJ*, 709, 937
 Greene, J. E., Zakamska, N. L., Ho, L. C., & Barth, A. J. 2011, *ApJ*, 732, 9
 Hainline, K. N., Hickox, R. C., Greene, J. E., et al. 2014, *ApJ*, 787, 65
 Harrison, C. M., Alexander, D. M., Swinbank, A. M., et al. 2012, *MNRAS*, 426, 1073
 Heckman, T. M., Miley, G. K., van Breugel, W. J. M., & Butcher, H. R. 1981, *ApJ*, 247, 40
 Hewett, P. C., & Wild, V. 2010, *MNRAS*, 405, 2302
 Ho, L. C., Goldoni, P., Dong, X.-B., Greene, J. E., & Ponti, G. 2012, *ApJ*, 754, 11
 Hu, C., Wang, J.-M., Ho, L. C., Chen, Y.-M., Bian, W.-H., & Xue, S.-J. 2008, *ApJ*, 683, L115
 Husemann, B., Wisotzki, L., Sánchez, S. F., & Jahnke, K. 2013, *A&A*, 549, 43
 Johnson, S. D., Chen, H.-W., & Mulchaey, J. S. 2015, *MNRAS*, 452, 2553
 Kim, M., Ho, L. C., Lonsdale, C. J., Lacy, M., Blain, A. W., & Kimball, A. E. 2013, *ApJ*, 768, L9
 Komossa, S., Xu, D., Zhou, H., Storchi-Bergmann, T., & Binette, L. 2008, *ApJ*, 680, 926
 Laor, A. 1997, *ApJ*, 477, 93
 Laor, A. 2000, *ApJ*, 543, L111
 Lawrence, A., Warren, S. J., Almaini, O., et al. 2007, *MNRAS*, 379, 1599
 Liu, G., Zakamska, N. L., Greene, J. E., Nesvadba, N. P. H., & Liu, X. 2013a, *MNRAS*, 430, 2327
 Liu, G., Zakamska, N. L., Greene, J. E., Nesvadba, N. P. H., & Liu, X. 2013b, *MNRAS*, 436, 2576
 Marziani, P., Sulentic, J. W., Zwitter, T., Dultzin-Hacyan, D., & Calvani, M. 2001, *ApJ*, 558, 553
 McIntosh, D. H., Rieke, M. J., Rix, H.-W., Foltz, C. B., Weymann, R. J. 1999, *ApJ*, 514, 40
 Mulchaey, J. S., Wilson, A. S., & Tsvetanov, Z. 1996, *ApJ*, 467, 197
 Nelson, C. H., Weistrop, D., Hutchings, J. B., et al. 2000, *ApJ*, 531, 257
 Nesvadba, N. P. H., Lehnert, M. D., De Breuck, C., Gilbert, A. M., & van Breugel, W. 2008, *A&A*, 491, 407
 Netzer, H., Lira, P., Trakhtenbrot, B., Shemmer, O., & Cury, I. 2007, *ApJ*, 671, 1256
 Netzer, H., Shemmer, O., Maiolino, R., Oliva, E., Croom, S., Corbett, E., & di Fabrizio, L. 2004, *ApJ*, 614, 558
 Perna, M., Brusa, M., Cresci, G., et al. 2015, *A&A*, 574, A82
 Plotkin, R. M., Shemmer, O., Trakhtenbrot, B., et al. 2015, *ApJ*, 805, 123
 Risaliti, G., Salvati, M., & Marconi, A. 2011, *MNRAS*, 411, 2223
 Runnoe, J. C., et al. 2013a, *MNRAS*, 429, 135
 Runnoe, J. C., Ganguly, R., Brotherton, M. S., & DiPompeo, M. A. 2013b, *MNRAS*, 433, 1778
 Saito, Y., Imanishi, M., Minowa, Y., et al. 2015, *PASJ*, arXiv:1510.02522
 Schmitt, H. R., Donley, J. L., Antonucci, R. R. J., et al. 2003, *ApJ*, 597, 768
 Schneider, D. P., et al. 2010, *AJ*, 139, 2360
 Shang, Z., Wills, B. J., Robinson, E. L., et al. 2003, *ApJ*, 586, 52
 Shemmer, O., et al. 2004, *ApJ*, 614, 547
 Shemmer, O., & Lieber, S. 2015, *ApJ*, 805, 124
 Shen, Y. 2013, *BASI*, 41, 61
 Shen, Y., et al. 2011a, *ApJS*, 194, 45

- Shen, Y., Greene, J. E., Strauss, M. A., Richards, G. T., & Schneider, D. P. 2008, *ApJ*, 680, 169
- Shen, Y., & Ho, L. C. 2014, *Nature*, 513, 210
- Shen, Y., & Liu, X. 2012, *ApJ*, 753, 125
- Shen, Y., Liu, X., Greene, J. E., & Strauss, M. A. 2011b, *ApJ*, 735, 48
- Simcoe, R. A., et al. 2010, *SPIE Conf.*, 7735, 38
- Skrutskie, M. F., et al. 2006, *AJ*, 131, 1163
- Stern, J., & Laor, A. 2012a, *MNRAS*, 423, 600
- Stern, J., & Laor, A. 2012b, *MNRAS*, 426, 2703
- Stockton, A., & MacKenty, J. W. 1987, *ApJ*, 316, 584
- Sulentic, J. W., Bachev, R., Marziani, P., Negrete, C. A., & Dultzin, D. 2007, *ApJ*, 666, 757
- Sulentic, J. W., Repetto, P., Stirpe, G. M., Marziani, P., Dultzin-Hacyan, D., & Calvani, M. 2006, *A&A*, 456, 929
- Sulentic, J. W., Stirpe, G. M., Marziani, P., Zamanov, R., Calvani, M., & Braitto, V. 2004, *A&A*, 423, 121
- Sulentic, J. W., Zwitter, T., Marziani, P. & Dultzin-Hacyan, D. 2000, *ApJ*, 536, L5
- Sun, J., & Shen, Y. 2015, *ApJ*, 804, L15
- Vanden Berk, D. E., Richards, G. T., Bauer, A., et al. 2001, *AJ*, 122, 549
- Vestergaard, M., & Peterson, B. M. 2006, *ApJ*, 641, 689
- Villar-Martín, M., Humphrey, A., Delgado, R. G., Colina, L., & Arribas, S. 2011, *MNRAS*, 418, 2032
- Wang, T., Brinkmann, W. & Bergeron, J. 1996, *A&A*, 309, 81
- Whittle, M. 1985, *MNRAS*, 213, 1
- Wills, B. J., & Browne, I. W. A. 1986, *ApJ*, 302, 56
- Wills, B. J., Laor, A., Brotherton, M. S., Wills, D., Wilkes, B. J., Ferland, G. J., & Shang, Z. 1999, *ApJ*, 515, L53
- Wilson, J. C., Henderson, C. P., Herter, T. L., et al. 2004, *Proc. SPIE*, 5492, 1295
- Yuan, M. J., & Wills, B. J. 2003, *ApJ*, 593, L11
- Zamanov, R., Marziani, P., Sulentic, J. W., Calvani, M., Dultzin-Hacyan, D., & Bachev, R. 2002, *ApJ*, 576, L9
- Zhang, K., Dong, X., Wang, T., Gaskell, C. M. 2011, *ApJ*, 737, 71
- Zhang, K., Wang, T.-G., Gaskell, C. M., & Dong, X.-B. 2013, *ApJ*, 762, 51
- Zuo, W., Wu, X.-B., Fan, X., Green, R., Wang, R., & Bian, F. 2015, *ApJ*, 799, 189